Power Electronic Systems
Laboratory

Proceedings of the IEEE International Conference on Power Electronics, Drives & Energy Systems (PEDES 2016), Trivandrum, India, December 14-17, 2016

Weight Optimization of an Axial-Flux PM Machine for Airborne Wind Turbines

I. Subotic,
C. Gammeter,
A. Tüysüz,
J. W. Kolar

Eidgenössische Technische Hochschule Zürich
Swiss Federal Institute of Technology Zurich

Weight Optimization of an Axial-Flux PM Machine for Airborne Wind Turbines

Ivan Subotic, Christoph Gammeter, Arda Tüysüz, Johann Walter Kolar
Power Electronic Systems Laboratory (PES), ETH Zurich,
8092 Zurich, Switzerland
e-mail: subotic@lem.ee.ethz.ch

***Abstract*—This paper considers the weight optimization of an axial-flux machine (AFM) for airborne wind turbines (AWT). It employs combined electrical, thermal and structural (mechanical) analytical models, which allow a fast evaluation of machine performance. Therefore, instead of introducing cost functions, the complete machine design space can be considered. The machines are shown in a performance space from which a Pareto limit can be clearly identified, and an optimal machine chosen for any given application. Optimization results yield a maximum power-to-weight ratio of 6.4 kW/kg including structural (non-electrical) parts, at an efficiency of 95 % and rated speed of 3200 rpm, which is unparalleled by commercial machines, or those reported in literature. Analytical models are verified by FEM simulations, and a prototype of the optimal AFM is built in order to experimentally confirm the results.**

Keywords*—*analytical machine models, axial-flux machine (AFM), weight optimization, wind power generation, airborne wind turbine (AWT), Pareto optimization, renewable energy.

I. Introduction

An airborne wind turbine (AWT) is a wind turbine (WT) that is not rigidly fixed to the ground. At present most of the AWT systems are either kite- [1] or balloon-based [2]. Fig. 1 depicts a kite-based AWT, which is described in [1]. Its operating principle is similar to that of a standard WT. Wind energy is used to provide the same rotational motion (indicated by blue surfaces in Fig. 1) of either rotor blades (in standard WTs - Fig. 1a) or the whole kite (in AWTs - Fig. 1b). An electric machine attached either directly on the centre hub of the rotor blades (Fig. 1a) or on the kite (Fig. 1b) opposes that motion, and, therefore, operates as a generator.

Compared to standard WTs, AWTs do not require a supporting tower or long rotor blades, thus they have much lower weight for the same output power, leading to a lower cost of utilized materials, and competitiveness with modern, commercially available conventional WTs.

In order to lower the investment cost per produced power, conventional WTs have to be designed for higher rated power (higher towers and larger diameters of the area swept by the blades). However, this trend is likely to stop when a height limit is reached, which is imposed by mechanical construction. This limit is incomparably higher in AWTs, which identifies them as a possible solution for mass energy production by harnessing high-altitude winds.

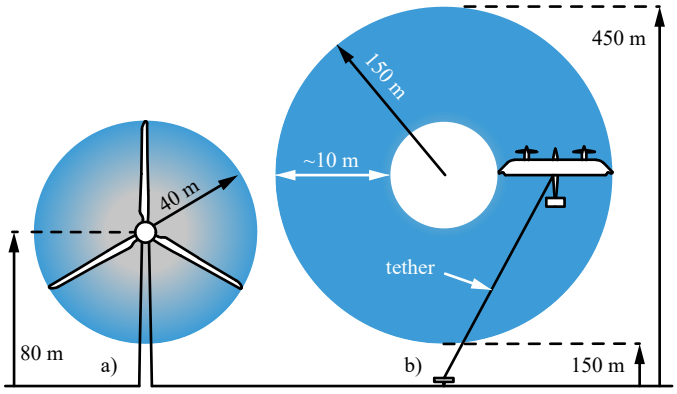

Fig. 1. a) 750 kW standard WT, b) 600 kW AWT: the kite emulates the behaviour of rotor blades' tips. Inverter and a dc/dc converter are placed on the kite. The energy is transmitted to the ground by a flexible HVDC tether. The approximate dimensions are taken from [3].

Although these advantages of AWTs were noticed already more than four decades ago [4-5], only recent advances in power and control systems and light-weight materials made this technology feasible. This introduced the necessity of weight versus efficiency optimization of its components [1], of which the machine is given the particular focus in this paper.

Optimization is commonly performed by minimizing cost functions. However, a cost function is not always trivial to define, especially when a multitude of performance indices are to be considered such as efficiency and power-to-weight ratio. Moreover, the minimization of a cost function may also bear the risk of converging to a local optimum.

An alternative is the direct grid search method, which considers the complete design space, and by doing so, does not rely on any cost function. By mapping the performance of every single machine design in a discretized design space to a performance space, this method can easily identify a Pareto-optimum group of machine designs. The most suitable machine can then be selected from the group of Pareto-optimum designs, based on the specific trade-offs of the application at hand.

The direct grid search can be achieved by utilizing either finite element analysis (FEA), analytical formulas, or their combination. Although methods employing FEA are capable of direct grid search [6], their high computational time limits the number of designs that can be considered. Thus, analytical

978-1-4673-8888-7/16/$31.00 ©2016 IEEE

models, which are well-established for AFMs, are preferred for this type of optimization [1]. Optimization of machines for AWTs is already considered in [7]. Unlike [7], this paper focuses just on AFM, and provides a comprehensive analysis of all its types, including those employing phase group stator windings.

This paper is organised as follows. Section II defines a design space (i.e. "the grid") of all machines that are considered in the optimization process. The analytical models on which the optimization is based are detailed in Section III. Optimization results are presented in Section IV, while the manufacturing process of the prototype machine is described in Section V. Analytical and FEM results are verified by experiments in Section VI. Section VII concludes the paper.

II. Defining a Machine

A. Rotor design

Two rotor types are considered in this work. One employs axially magnetized magnets (phase shift between magnets is 180 degrees) and this type commonly has a back iron, which strengthens the flux towards the stator, cf. Fig. 2a. The other rotor type employs a Halbach configuration of magnets, which means that the phase shift between magnets is 90 degrees. This rotor type cannot prosper from a back iron, thus is omitted, Fig. 2b. Table I summarizes the parameters that define the rotor.

Only neodymium iron boron (NdFeB) is considered for permanent-magnet material, and cobalt iron (CoFe) for the back iron. Although silicon iron (SiFe) has 4% lower mass density than CoFe, it is outperformed by CoFe in terms of weight reduction, as it has a higher saturation flux density (2.3 T compared to 1.8 T of SiFe). Moreover, the focus is only on double rotor - single stator AFMs (Fig. 2c), which outperform single rotor AFMs with single or double stator in terms of power-to-weight ratio [7]. At last, machine stacking (adding additional stators and rotors in axial direction) is not considered as the maximum disk outer radius r_2 is not limited.

B. Stator design

Air core stators feature low weight, no iron losses, easy manufacturing and no cogging torque [9]. Therefore, only this stator type is considered in the paper.

The stator can be made with distributed windings (DW - Fig. 2d), traditional concentrated windings (TCW - Fig. 2e) or phase group concentrated windings (PGCW - Fig. 2f). Design degrees of freedom that define the stator are summarised in Table II.

It should be noted that although the number of coils (Q) is a degree of freedom, air core stators with DW and PGCW have a clear optimum that maximizes fundamental winding factor at $Q = 3p$ and $Q = 2p \pm 1$, respectively, where p is the number of rotor pole pairs.

Finally, for quick referencing and clearer view all fixed choices together with parameters that are limited by mechanical construction or manufacturability (e.g. air gap) are summarised in Table III for all the considered designs.

Tables I-III completely define all considered AFMs, and are sufficient to form a discretised design space for the direct grid search method.

TABLE I. Rotor Degrees of Freedom and Their Considered Values

Degree of freedom	Considered values (or designs)
Magnetization type	Axial with back iron (Fig. 2a), Halbach without iron (Fig. 2b)
Pole pair number [-]	$p = 19 + \{0, 1, 2, \ldots 7\}$
Disk inner radius [mm]	$r_1 = 80 + 10 \cdot \{0, 1, 2, \ldots 5\}$
Disk outer radius [mm]	$r_2 = 90 + 5 \cdot \{0, 1, 2, \ldots 14\}$
Permanent magnet height [mm]	$h_m = \{1, 2, 3, 4, 5\}$
Pole coverage of axial magnets [-]	$\alpha_p = \{0.5, 0.6, 0.7, 0.8\}$

TABLE II. Stator Degrees of Freedom and Their Considered Values

Degree of freedom	Considered values (or designs)
Winding type	Distributed (Fig. 2c), Traditional concentrated (Fig. 2d), Phase group concentrated (Fig. 2e)
Number of coils	$Q = 36 + 3 \cdot \{0, 1, 2, \ldots 14\}$
Coil height [mm]	$c_h = 80 + 10 \cdot \{0, 1, 2, \ldots 5\}$
Fractional coil width [-]	$c_{\omega,\mathrm{frac}} = \frac{2c_\omega}{c_{\omega,\max}} = 0.45 + 0.1 \cdot \{0, 1, \ldots 4\}$
Coil material	Copper, Aluminium
Current waveform	Sinusoidal (BLAC), Block (rectangular – BLDC)

TABLE III. Fixed Parameters of the Machine

Fixed parameter	Value (or design)
Machine type	Dual rotor with single stator,
Number of stacks	1
Stator type	Coreless
Permanent magnet material	NdFeB
Back iron material	CoFe (with Halbach not required)
Fill factor [-]	$k_{Cu} = 0.55$ for distributed windings, $k_{Cu} = 0.85$ for concentrated windings
Air gap [mm]	1
Back iron height	h_{Fe} is just sufficient to avoid saturation

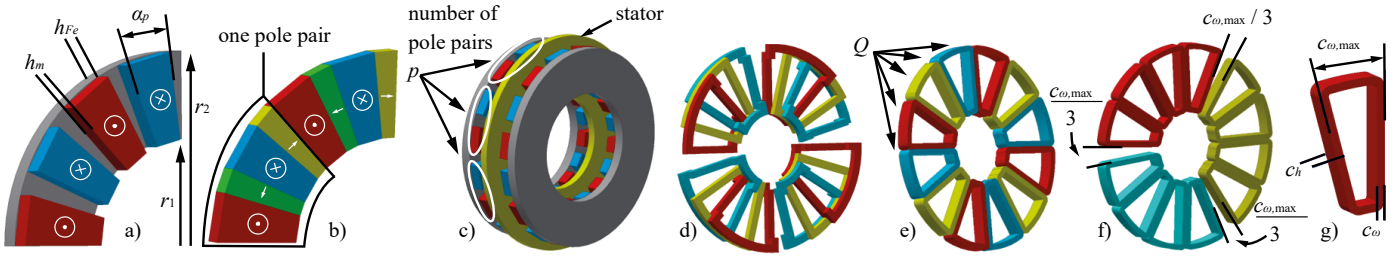

Fig. 2. a) quarter of rotor with axial magnetization and back iron, b) quarter of rotor with Halbach magnetization, c) dual rotor AFM, d) stator with distributed windings (given for $Q = 12$), e) stator with traditional concentrated windings (given for $Q = 12$), f) stator with phase group concentrated windings (given for $Q = 12$), g) single stator coil. In Figs. 2d), 2e) and 2f) coils with the same colour belong to the same phase.

III. Machine Modelling

Once a machine is defined (Section II), its power-to-weight ratio is assessed analytically. In order to accomplish this, a combination of three types of analytical models is required: electro-magnetic, thermal and structural.

A. Electro-magnetic modelling

As already noted, analytical modelling of air cored AFM is nowadays well known. The process initiates with determination of spatial distribution of rotor B-field in the machine ($\vec{B}$ (x,y,z)). This field depends on geometry of the rotor discs and the distance between them, and is completely independent of the stator. Although its derivation is complex, its final form for axial magnetization with back iron can be found in [10], while for Halbach magnetization it is given in [11]. These forms are utilized in this work, and in what follows it is considered that the B-field is known. A graphical representation of B-field z-component distribution in the middle of the air gap for one of the considered machines utilizing Halbach magnetization is given in Fig. 3.

Once the B-field is known, the required armature current for a required torque can be obtained in a straightforward manner by utilizing Lorentz force F,

$$\vec{T} = \vec{r} \times \vec{F} = \vec{r} \times (i \cdot \vec{l} \times \vec{B}) , \quad (1)$$

where l is a length of the conductor, r its distance from the centre of rotation and i applied current.

Only tangential force component is of interest. Therefore, it can be written as

$$T_\varphi = r \cdot F_\varphi = r \cdot i_r B_z l . \quad (2)$$

From (2) it follows that only current in radial direction (i_r) generates torque, thus, it is evident that end windings do not contribute to the torque production.

The field B_z is not constant in the air gap (Fig. 3). Moreover, observed from stator reference frame it rotates at rotational speed ω. If angle of rotation is introduced as

$$\theta = \omega \cdot t , \quad (3)$$

an infinitesimal torque element produced by current from phase a can be obtained from (2) as

$$\mathrm{d}T_{a\varphi} = r \cdot \mathrm{d}F_{a\varphi} = r \cdot \frac{\pm i_{a,coil} \cdot \cos(\varphi)}{k_\omega \cdot \omega_\omega \cdot \omega_h} B_z(r, \varphi - \theta, z) \cdot \mathrm{d}V_a , \quad (4)$$

where $i_{a,\,coil}$ is total current of phase a that flows through the cross-section of a coil, and $J_{a,\varphi} = \dfrac{\pm i_a \cdot \cos(\varphi)}{k_\omega \cdot \omega_\omega \cdot \omega_h}$ is the radial component of its density. The sign ± signifies that direction of the current i_a (from the inner towards the outer machine edge, or vice versa) has to be taken into account. The total torque of phase a is obtained by spatial integration of the infinitesimal torque elements from (4),

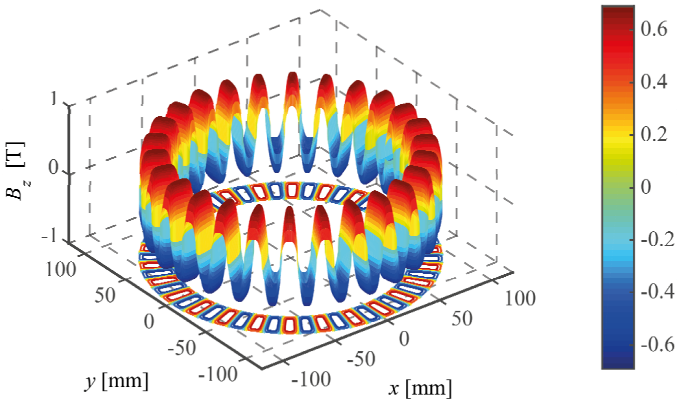

Fig. 3. Analytical calculation of B-field distribution in the middle of the air gap for the case of rotors with Halbach magnets with $p = 26$, $r_1 = 90$ mm and $r_2 = 115$ mm (the prototype machine – see Section V-A).

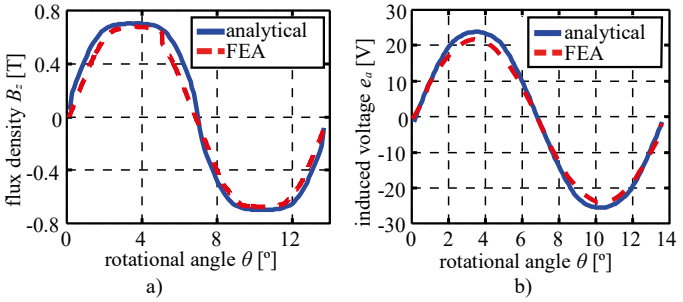

Fig. 4. Comparison of analytical and FEA results for: a) B-field distribution in the middle of the air gap, b) open-circuit induced voltage (e_a) in machine phase a, at the speed of 300 rpm for the prototype machine (Section V-A).

$$T_{a\varphi} = \iiint_{V_a} \mathrm{d}T_{a\varphi} , \quad (5)$$

where V_a is volume of the active (radial) part of the windings belonging to phase a (does not include end windings).

If the machine is driven by balanced three-phase currents, its total average torque over its electric period t_p is governed by

$$T_{\varphi\,avg} = 3T_{a\varphi\,avg} = \frac{1}{t_p} 3 \int_{t=0}^{t=t_p} T_{a\varphi} \, \mathrm{d}t . \quad (6)$$

Now, if the average torque is already set as a requirement (12.5kW in this paper), a machine phase a current can be obtained from (4)-(6). Once machine current is known, stator conduction losses can be calculated from

$$P_{cond} = 3RI_{a\,rms}^2 , \quad (7)$$

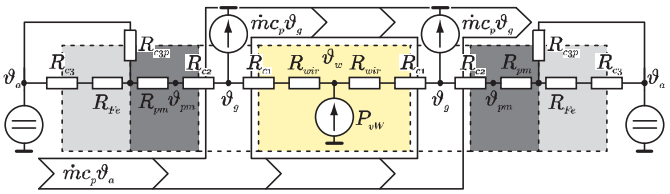

Fig. 5. Thermal model of a dual rotor AFM. Parameters R_{c1}, R_{c2}, R_{c3} and R_{c3p} are convective thermal resistances from ambient air to surfaces of: stator, magnets, back iron and rotor peripheral edge, respectively. Parameters $R_{\omega ir}$, R_{pm} and R_{Fe} are conduction thermal resistances of: windings, magnets and back iron, respectively.

where R is obtained based on coil dimensions. These, together with stator proximity losses, form total AFM losses from which efficiency can be obtained.

Finally, attaining knowledge on open-circuit induced phase voltage e_a is very valuable for determining performance of a machine, and it can be obtained from the power balance equation,

$$e_a \cdot i_a = T_{a\varphi} \cdot \omega \,, \tag{8}$$

where i_a is current of phase a that flows through a single wire of a coil.

The analytical models are verified by FEM simulations and a sample of the results is shown in Fig. 4. It can be seen that the peak error is around 10% which yields acceptable accuracy.

B. Thermal modelling

Thermal models give insight on machine internal temperatures. Machines that overheat during the operation feature degradation of lifetime and electro-magnetic properties. Thus, thermal limits must be included, and here they are chosen to be 125˚C for the windings and 90˚C for the magnets. Machine designs that surpass this limit get discarded.

Analytical thermal steady state modelling of double rotor AFMs is at present well known [9]. Here a lumped parameter thermal network, depicted in Fig. 5, is employed for the optimization process. In order to accelerate execution time of the model, it can be assumed that rotor temperature is equal to air temperature in the air gap. Now, parameters R_{c2}, R_{c3}, R_{c3p}, R_{pm} and R_{Fe} cease to influence the system, and the model gets reduced to its central part (dyed in yellow in Fig. 5).

Winding conduction resistance is governed by

$$R_{\omega ir} = \frac{l}{A_{\omega ir} \cdot k} \,, \tag{9}$$

where $A_{\omega ir} = (r_1^2 + r_2^2)\pi$ is stator cross-section area, $l = 0.5 \cdot \omega_h$ and k is thermal conductivity of stator material.

Convection resistance is governed by

$$R_c = \frac{1}{A_c \cdot h} \,, \tag{10}$$

where

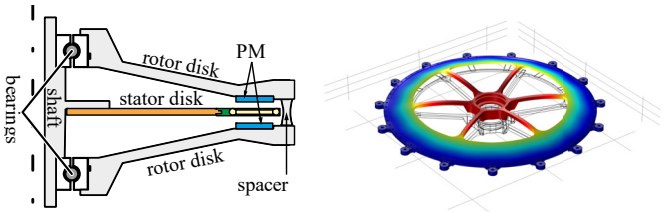

a) b)

Fig. 6. a) Sectional drawing of an AFM including electromagnetically inactive parts. b) FEM simulation of rotor bending caused by magnets' attraction forces.

$$h = \frac{k \cdot \overline{Nu}_{s,a}}{2\pi v \rho \bar{r}} \quad \text{and} \quad \overline{Nu}_{s,a} = 0.333 \frac{\dot{m}}{2\pi v \rho \bar{r}} \,. \tag{11}$$

Parameters k, v and ρ are air thermal conductivity, air kinematic viscosity and air density, respectively. Parameter $\dot{m}$ is air mass given by

$$\dot{m} = \dot{V} \cdot \rho \,, \tag{12}$$

where $\dot{V}$ is an inrush air volume flow, for which a value of 7 dm^3/s is here assumed.

At last, air gap air temperature θ_g and stator temperature θ_s can be obtained from (13) and (14), respectively.

$$\frac{P_{loss,tot}}{2} = \dot{m} c_p (\theta_g - \theta_a) \tag{13}$$

$$\frac{\theta_s - \theta_g}{R_{\omega ir} + R_{c1}} = \dot{m} c_p (\theta_g - \theta_a) \tag{14}$$

It should be noted that electro-magnetic and thermal models are mutually dependant through the temperature dependencies of remnant flux density of the permanent magnets and conductivity of the windings. Thus, modelling process of each machine demands several iterations.

C. Structural modelling

Once machine electro-magnetic and thermal analysis is performed, its structural weight is assessed. Structural modelling is essential in order to minimize passive weight as it influences the overall power-to-weight ratio. Machine mechanical structure is designed to withstand three types of stress: torque (shear force), centrifugal (tensile) force and magnetic attractive force (bending stress).

Simple analytical mechanical models [12] are employed in order to provide a basic structural design (Fig. 6a), and rough dimensions for the optimization process. Subsequently, fine refinement of the design is performed by FEM simulations, one of which is shown in Fig. 6b. It increased the power-to-weight ratio from 5.8 kW/kg (Fig. 7) to 6.4 kW/kg at efficiency of 95% and speed of 3200 rpm.

IV. Optimization Results

Analytical models given in Section III provide information on the power-to-weight ratio and the efficiency of all the AFMs defined in Section II. A power-to-weight ratio versus efficiency trade-off is known as Pareto front graph, and it is indispensable

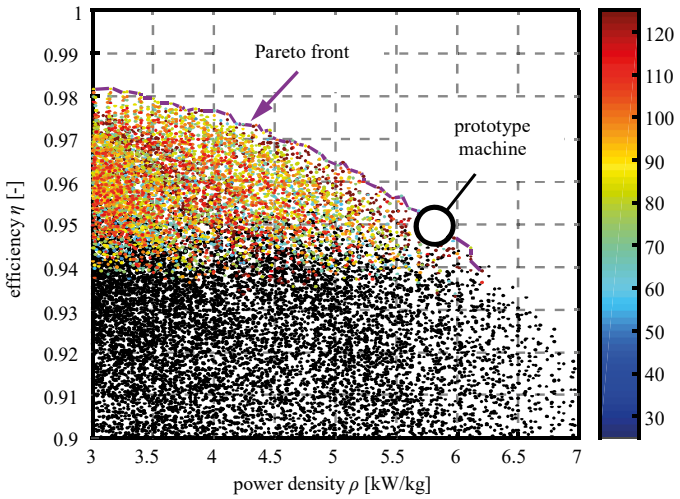

Fig. 7. Pareto graph of the machines defined in Section II. Machines that overheat during the operation are dyed in black.

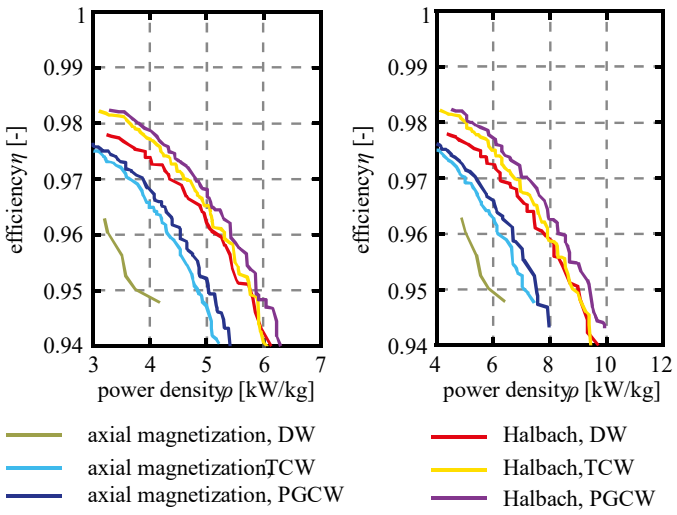

Fig. 8. Pareto fronts of all the AFMs defined in Section II: including (left side), excluding structural weight (right hand side).

for selection of an optimal machine design. Therefore, data on efficiency and power-to-weight ratio of all the machines is given in the form of a single Pareto front graph (Fig. 7), where each machine design is represented with a single data point.

Machines that overheat during the operation (winding or magnet temperature over 125˚C or 90˚C, respectively) are dyed in black. Purely from Fig. 7, a machine design that achieves a power-to-weight ratio of 5.8 kW/kg (6.4 kW/kg after fine structural refinement by FEM simulations, cf. Fig. 6b) at an efficiency of 95% is taken as optimal and chosen to be manufactured as a prototype (Section V).

In Fig. 8 Pareto fronts of different AFM types (both with and without structural mass) are shown together in order to allow a comparison. It can be seen that AFMs with concentrated windings (Figs. 2e), 2f)) outperform those with distributed windings (Fig. 2d)), which is attributed to shorter end windings and higher fill factor k_ω (Table III). It is also clear that rotor disks with magnets in Halbach configuration (Fig. 2b)) yield better performance than those with purely axial magnets (Fig. 2a)), as they feature higher air gap flux density with the same weight.

It should be noted that post-processing of results revealed that employing aluminium instead of copper as a winding material always reduces performances. The reasoning behind this is that for the same current rating aluminium coils demands an increased coil height (and increased distance between the two rotors) compared to their copper counterparts, due to their lower electrical conductivities.

V. Prototype Machine

A. Chosen dimensions and design parameters

As already stated, a machine is completely defined by Tables I-III. Values from these tables that match the prototype machine (which yields power-to-weight density of 6.4 kW/kg and the efficiency of 95%) are given in what follows.

The prototype machine has a dual rotor and a single stator. The rotor is separated from the stator by an air gap of 1 mm. It utilizes NdFeB magnets in a Halbach configuration without a back iron. It has 26 pole pairs (p). Its inner radius is $r_1 = 90$ mm, while the outer radius is $r_2 = 115$ mm. Magnet height is $h_m = 4$ mm, and its pole coverage is $\alpha_p = 0.6$.

The stator is coreless and it utilizes phase group concentrated windings with a fill factor of $k_{Cu} = 85\%$. It has 51 copper coils. Coil height is 3.5 mm, while its fractional width is $c_{\omega,\text{frac}} = 0.65$. It is meant for operation with sinusoidal currents.

The given values are sufficient for the machine manufacturing process.

B. Stator manufacture

The stator consists of three parts: concentrated windings, a thin, CNC-milled aluminium rim and epoxy between them.

At first, a custom made tool is CNC milled and employed to roll and shape a rectangular wire. When this is done, dc current of 30 A is applied through the wire which melts its self-bonding layer and stiffens the coil. A coil obtained by the described process is presented in Fig. 9a.

In order to keep the concentrated windings in position, they are potted in epoxy (Loctite Hysol 9497) together with the aluminium rim. A sealed Teflon mould (one half of it is shown in Fig. 9b) is utilized in order to avoid any air inclusions. Vacuum is produced by a vacuum pump and the pressure is monitored on a barometer. Fig. 9c shows the potted stator mounted on a shaft.

C. Rotor manufacture

Each of the two identical rotors consists of ball bearings (a hybrid ceramic type is employed to prevent common mode current flow) an aluminium shield and a magnet disk. The shield is milled on a CNC machine while the trapezoidal magnets for Halbach array are bought. At first, the magnets are positioned on a thin Teflon mould, below which an iron plate is placed. Attraction forces of the magnets are higher on the iron plate than among themselves, which ensures that the magnets do not collide during the assembly process.

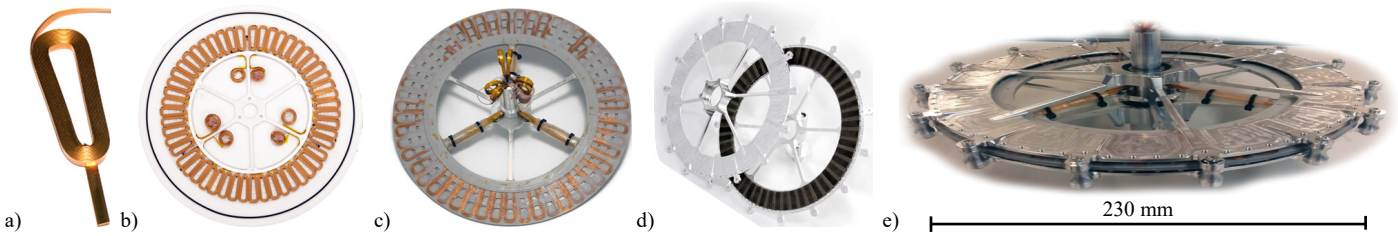

Fig. 9. Prototype machine parts: a) a coil produced by a custom made winding tool, b) stator coils placed on a potting mould, c) potted stator, d) two assembled rotors, e) completely assembled AFM.

When all the magnets are arranged on the mould, a two-component adhesive (the same one as for the stator potting) is applied on the aluminium shield and it is placed on the top of the magnets. Clamps are employed to apply pressure between the shield and the mould. After a cure time of 24h they are released, and the rotor is complete (Fig. 9d).

The fully assembled machine is shown in Fig. 9e. It weights m_{tot} = 2.065 kg, which is in good accordance with the value predicted by simulations (2.075 kg).

VI. Experimental Results

The prototype machine is experimentally tested in order to verify the analytical and FEM results. Waveforms that are chosen for the comparison with analytical and FEM results (Fig. 4b) are open-circuit induced phase voltages (e_a, e_b, and e_c) and corresponding flux linkages. As already noted, open-circuit induced phase voltage is one of the most important indicators of machine performances as it directly provides information (based on (8)) on ratio between machine current and a mechanical power.

The prototype AFM is mechanically coupled to an off-the-shelf machine which is utilized to spin the AFM to a desired speed. For the experiment a value of 300 rpm is selected (to allow a comparison with Fig. 4). The AFM open-circuit induced voltages e_a, e_b and e_c are measured and depicted in Fig. 10a. Their correlation with flux linkages is governed by (15). Thus, by integration of these waveforms, flux linkages are obtained (Fig. 10b). A maximum value of $29 \cdot 10^{-3}$ Wb is obtained, which is in good accordance with a value predicted by FEM analysis.

$$e = -\frac{\mathrm{d}\varphi}{\mathrm{d}t}, \tag{15}$$

VII. Conclusion

In this paper, a multi-objective (Pareto) optimization of an axial-flux machine (AFM) for airborne wind turbines (AWTs) is performed. The optimization is based on electro-magnetic, thermal and structural analytical models, which are verified by FEM simulations. The direct grid search method is utilized; thus the complete design space is covered. The machines' performances are revealed in the performance space with a clearly pronounced Pareto front, based on which the optimal machines can be identified for different applications.

Optimization results yield a power-to-weight ratio of 6.4 kW/kg (2.9 kW/lb) at an efficiency of 95% and a rated speed of 3200 rpm, which is unparalleled by commercial machines, or those reported in literature. The optimal AFM is manufactured in order to verify the results. The AFM total weight of 2.065 kg is reported and is in good accordance with the value predicted by simulations (2.075 kg). Initial measurements verify the key design aspects such as the electro-magnetic performance. Future work will focus on the verification of the thermal model as well.

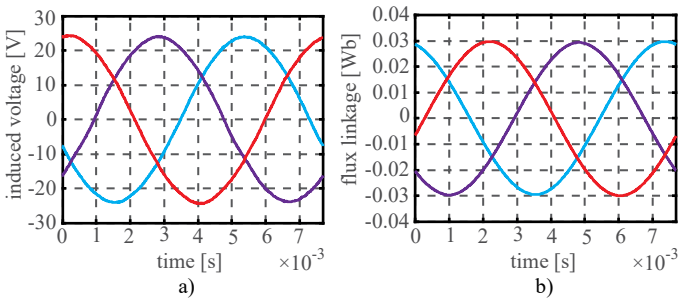

Fig. 10. Experimental results of: a) open-circuit induced voltages e_a, e_b and e_c at the speed of 300 rpm, b) flux linkage of the phases *a*, *b* and *c*.

References

[1] J. W. Kolar et al., "Conceptualization and multiobjective optimization of the electric system of an airborne wind turbine," *IEEE Journal of Emerging and Selected Topics in Power Electronics*, vol. 1, no. 2, pp. 73-103, 2013.

[2] J. Adhikari and S. K. Panda, "Overview of high altitude wind energy harvesting system," *Proc. of the 5th Int. Conf. on Power Electronics Systems and Applications (PESA)*, Hong Kong, China, 2013.

[3] Makani Power, Accessed June 2016, [Online], Available: http://www.google.com/makani.

[4] P. R. Payne and C. McCutchen, "Self-erecting windmill," *patent US 3987987A*, 1976.

[5] M. L. Loyd, "Crosswind kite power," *J. Energy*, vol. 4, no. 3, pp. 106–111, 1980.

[6] A. Tüysüz, C. Zwyssig and J. W. Kolar, "A novel motor topology for high-speed micro-machining applications," *IEEE Trans. on Ind. Electronics*, vol. 61, no. 6, pp. 2960-2968, 2014.

[7] C. Gammeter, Y. Drapela, A. Tüysüz and J. W. Kolar, "Weight optimization of a machine for airborne wind turbines," *Proc. of the 40th IEEE Ind. Electronics Society Conf. (IECON)*, Dallas, Texas, 2014.

[8] J. O. Buøy, "Development of high efficiency axial flux motor for Shell eco-marathon," *Master Thesis at Norwegian University of Science and Technology*, 2013.

[9] J. F. Gieras, R. J. Wang and M. J. Kamper, "Axial flux permanent magnet brushless machines. 2nd edition," *Springer*, 2008.

[10] Y. Huang, B. Ge, J. Dong, H. Lin, J. Zhu and Y. Guo, "3-D analytical modeling of no-load magnetic field of ironless axial flux permanent magnet machine," *IEEE Trans. on Magnetics*, vol. 48, no. 11, pp. 2929-2932, 2012.

[11] W. K. Thompson, "Three-dimensional field solutions for multi-pole cylindrical Halbach arrays in an axial orientation," *Report, NASA Glenn Research Centre*, Cleveland, Ohio, 2006.

[12] M. A. Mueller, A. S. McDonald and D. E. Macpherson, "Structural analysis of low-speed axial-flux permanent-magnet machines," *IEE Proc. - Electric Power Applications*, vol. 152, no. 6, pp. 1417-1426, 2005.